JOURNAL OF GEOPHYSICAL RESEARCH: SPACE PHYSICS, VOL. 118, 4895–4905, doi:10.1002/jgra.50455, 2013

Comparison of TWINS and THEMIS observations of proton pitch angle distributions in the ring current during the 29 May 2010 geomagnetic storm

E. W. Grimes,[1,2] J. D. Perez,[1] J. Goldstein,[3,4] D. J. McComas,[3,4] P. Valek,[3,4] and D. Turner[2]

Received 10 February 2013; revised 13 July 2013; accepted 17 July 2013; published 8 August 2013.

[1] The first comparison between energy-dependent ion pitch angle distributions in the ring current deconvolved from Two Wide-angle Imagining Neutral-atom Spectrometers (TWINS) energetic neutral atom (ENA) images and measured by Time History of Events and Macroscale Interactions during Substorms (THEMIS) D and E during a magnetic storm on 29 May 2010 is shown. The ion intensities and energy spectra along the THEMIS path are also compared with those deconvolved from the TWINS ENA images. The global plots of the ion intensities show an asymmetric ring current in the early recovery phase consistent with the ASY/H index. The comparison between the in situ pitch angle distributions observed by THEMIS and those obtained here from TWINS ENA images lends credence to the global plots of pitch angle anisotropy provided by the TWINS data. The spatial dependence of the pitch angle anisotropy provides information relevant to ion precipitation and lifetimes of trapped ring current ions not available from in situ measurements.

Citation: Grimes, E. W., J. D. Perez, J. Goldstein, D. J. McComas, P. Valek, and D. Turner (2013), Comparison of TWINS and THEMIS observations of proton pitch angle distributions in the ring current during the 29 May 2010 geomagnetic storm, *J. Geophys. Res. Space Physics*, *118*, 4895–4905, doi:10.1002/jgra.50455.

1. Introduction

[2] The pitch angle distribution of particles trapped and precipitating on geomagnetic field lines is a fundamental characteristic of inner magnetospheric electrodynamics. For instance, anisotropies in the pitch angle distribution of precipitating ring current ions contribute to the losses of those ions into the atmosphere [*Kennel and Petschek*, 1966]. During geomagnetic storms, these losses can lead to drastically shorter recovery times than otherwise predicted [*Ebihara et al*., 2011]. Anisotropies in the pitch angle distribution of ions can also lead to the generation of electromagnetic ion cyclotron (EMIC) waves [*Xiao et al*., 2007] and affect the production of energetic neutral atoms (ENAs) [*Zheng et al*., 2008], e.g., the so-called low-altitude emissions (LAEs) [*Roelof*, 1987], observed in ENA images near the Earth's limb.

[3] In this study, we show the first comparison of deconvolved ion pitch angle distributions in the ring current with those measured by Time History of Events and Macroscale Interactions during Substorms (THEMIS). We also compare the ion intensities along the THEMIS path with those deconvolved from ENA images and compare the in situ spectra with the spectra from the global observations. The comparison between the in situ pitch angle distributions observed by THEMIS and those obtained here from Two Wide-angle Imagining Neutral-atom Spectrometers (TWINS) ENA images which shows good agreement lends credence to the global plots of pitch angle anisotropy provided by the TWINS data.

[4] In section 2, we describe the data sources followed by the relevant observations in section 3. The results are discussed in section 4 and summarized in section 5.

2. Data Sources

[5] The Two Wide-angle Imagining Neutral-atom Spectrometers (TWINS) mission is a NASA Explorer Mission-of-Opportunity consisting of two ENA instruments in widely separated Molniya orbits [*McComas et al*., 2009a]. Dual vantage points give TWINS a unique geometry to simultaneously measure the global distribution of ENAs in the ring current over a broad energy range (1–100 keV). *Goldstein et al*. [2012a, 2012b] have inferred the pitch angle anisotropy using stereo ENA images from TWINS. Through inversion techniques, we can extract the underlying ion intensity and pitch angle distributions from these ENA images. In this study, we focus upon ENA images from TWINS-2 early in the recovery of a storm on 29 May 2010 during a time period in which THEMIS D and E pass through the peak in the ring current ions.

[6] Prior to extracting the ion distribution, the TWINS images are statistically smoothed using a technique described in detail in Appendix A of *McComas et al*. [2012] and

[1]Physics Department, Auburn University, Auburn, Alabama, USA.
[2]Institute of Geophysics and Planetary Physics, Department of Earth and Space Sciences, University of California, Los Angeles, California, USA.
[3]Space Science and Engineering Division, Southwest Research Institute, San Antonio, Texas, USA.
[4]Physics Department, University of Texas, San Antonio, Texas, USA.

Corresponding author: J. D. Perez, Physics Department, Auburn University, 206 Allison Lab, Auburn, AL 36849, USA. (perez@physics.auburn.edu)

2169-9380/13/10.1002/jgra.50455

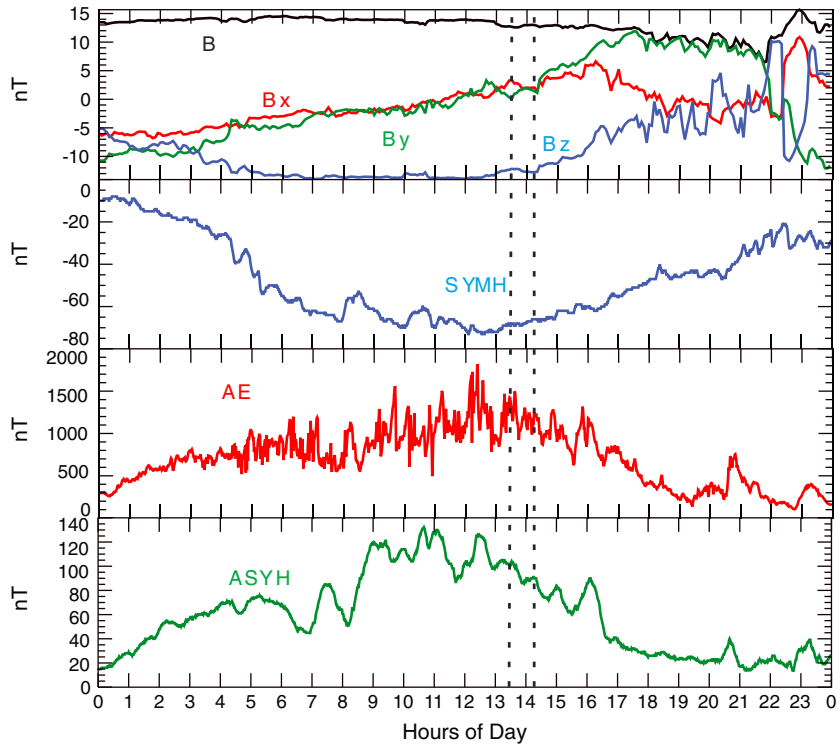

Figure 1. Interplanetary and geomagnetic conditions for 29 May 2010 taken from the OMNI web site, http://omniweb.gsfc.nasa.gov/omsc_min.html. The interplanetary magnetic field values are time shifted to correspond to the arrival at the magnetopause. This data set compiled by NASA's Space Physics Data Facility includes data from ACE, Wind, IMP 8, and Geotail satellite missions. The vertical dashed lines show the time interval in this study.

previously applied successfully to ENA images from IBEX [*McComas et al*., 2009b] and TWINS [*Valek et al*., 2010; *Grimes et al*., 2010; *Perez et al*., 2012].

[7] The intensity of energetic neutrals in pixel β of an ENA image, d_β [#neutrals/(cm^2 s sr eV)], assuming that the ENA reaches the observer without reabsorption and reemission, is the integral of the volume of the β^{th} pixel (4° × 4° for this study), expressed as

$$d_\beta = \iiint I(x,v,t)\sigma_{ex}(E)n(x)R_\beta(x)\mathrm{d}^3x$$

where $I(x,v,t)$ [#ions/(cm^2 s sr eV)] is the unknown ion intensity or directional differential number flux at the creation point of the ENA, $n(x)$ [#neutrals/cm^3] is the neutral hydrogen density, σ_{ex} [cm^2/#ions] is the energy-dependent charge-exchange cross section of protons with neutral hydrogen and neutral oxygen [*Barnett*, 1990], R_β [cm^{-2}] is the response function of the instrument, and d^3x [cm^3] is the pixel volume. In this study, since the observed quantity is the ENA intensity entering the instrument, the response function is merely the inverse of the pixel area. Information regarding the sensitivity of the detector has been folded into the analysis of the data as described in the previous paragraph and references given there. (This integral has been referred to as a line-of-site integral in previous treatments. See for example, *Brandt et al*. [1997]. The primary difference between our expression and equation (1) in *Brandt et al*. [1997] is that the equation given here is for a pixel and therefore includes an integral over the volume contributing ENAs to the particular pixel.) For each point in the integrals, the neutral hydrogen density is estimated using the model by *Østgaard et al*. [2003], and the geomagnetic field is modeled using *Tsyganenko and Sitnov* [2005]. The ion intensities are then extracted from the ENA images using an inversion technique based on *Wahba* [1990] in which the intensity is expanded in terms of tricubic B-splines [*deBoor*, 1978]. The expansion coefficients, $a_{i,j,k}$ [#ions/(cm^2 s sr eV)], are defined in the expression

$$I(r,\varphi,\cos\psi) = \sum_i \sum_j \sum_k a_{i,j,k} S_i(r) P_j(\varphi) S_k(\cos\psi)$$

where $I(r,\varphi,\cos\psi)$ is the ion intensity in the equation above for d_β for a fixed energy band and a fixed time interval; $S_i(r)$ are the radial splines; $P_j(\varphi)$ are periodic, angular (MLT) splines; and $S_k(\cos\psi)$ are the cosine of the equatorial pitch angle splines. The $a_{i,j,k}$ are obtained by solving a set of integral equations obtained from the minimization requirement

$$\delta(\chi^2 - \lambda P) = 0$$

[8] The χ^2, defined as

$$\chi^2 = \frac{1}{N}\sum_{\beta=1}^{N}\frac{(d_\beta - c_\beta)^2}{\sigma_\beta^2}$$

where N is the number of pixels, σ_β is the uncertainty in the measured intensity in the β^{th} pixel, and c_β is the calculated ENA intensity in the β^{th} pixel

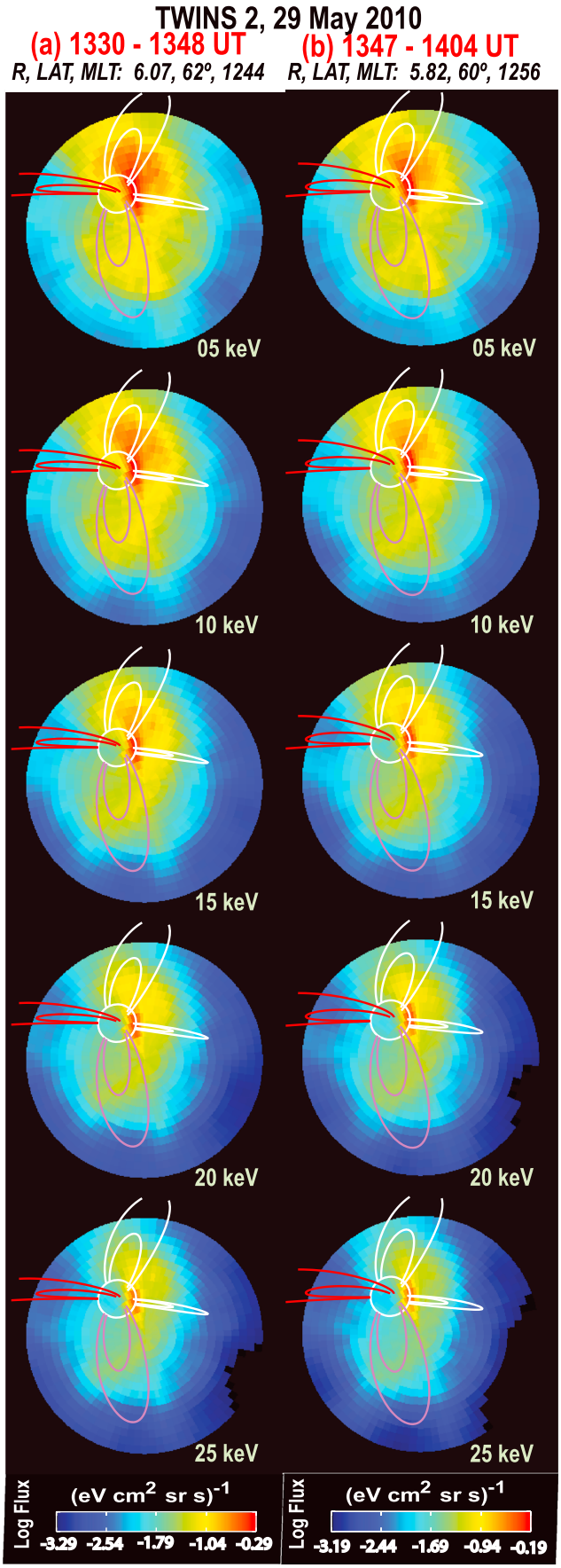

Figure 2

$$c_\beta = \sum_i \sum_j \sum_k D_{\beta,\{i,j,k\}} a_{i,j,k}$$

imposes the constraint of fitting the data, and the penalty function, P (not to be confused with the symbol P_j used for the periodic splines), requires that the solution be as smooth as possible. The expression for P is given in *Perez et al.* [2012]. Qualitatively, it means the smallest possible second derivative while still fitting the data. Thus, the λ parameter represents the balance between fitting the data and smoothness of the data. $D_{\beta,\{i,j,k\}}$ is the design matrix for the β^{th} pixel

$$D_{\beta,\{i,j,k\}} = \iiint \sigma_{ex}(E) n(x) S_i(r) P_j(\varphi) S_k(\cos\psi) R_\beta(x) \mathrm{d}^3 x$$

[9] To extract statistically significant information from the data, we then require that $\chi^2 = 1$ to determine λ. This technique, described in detail by *Perez et al.* [2012] and validated through cross comparison with data from THEMIS, allows us to calculate the equatorial pitch angle distribution of the ions producing ENAs in the ring current without prior information about the underlying ion distribution. Due to viewing geometry, only a portion of the ring current pitch angle distribution is observable by each individual TWINS instrument over the entire magnetospheric equator. When both spacecraft are operating simultaneously, we combine the data from both instruments in the inversion process to get a more complete view of the ring current ion population. In this study, we focus upon a region where comparison to THEMIS in situ measurements near the ion peak in the ring current can be made and where TWINS-2 sees an appreciable pitch angle range.

[10] The LAEs are modeled using a thick target approximation described in *Bazell et al.* [2010]. In this study, the LAEs are taken to come from an altitude of 600 km and are due to particles in and near a loss cone smoothed using a Gaussian function. In the procedure described in *Perez et al.* [2012] and used in this study, it is important to include the thick target approximation for the LAEs, but calculational tests have shown that there is little sensitivity to the chosen altitude for values from 300 km, determined by *Bazell et al.* [2010] to the 600 km used here.

[11] The Time History of Events and Macroscale Interactions during Substorms (THEMIS) mission [*Angelopoulos et al.*, 2008] is a multispacecraft NASA Explorer mission to study the physical processes behind magnetic reconnection and substorms in the magnetosphere. Each THEMIS spacecraft measures plasma ions from a few eV to 25 keV using an electrostatic analyzer (ESA) [*McFadden et al.*, 2008] and ions from 25 keV to 6 MeV using a solid state telescope (SST) [*Angelopoulos et al.*, 2008]. In this study, the measured particles are assumed to be protons for both TWINS and THEMIS.

Figure 2. TWINS-2 ENA at (a) 1330–1347 UT and (b) 1347–1404 UT. The images are 15-sweep, i.e., 17 min averages taken in energy intervals centered at 5, 20, 15, 20, and 25 keV with widths equal to the central energy. The ENA images are shown on a skymap projection with dipole field lines plotted at McIlwain L-shells, L = 4 and 8 R_E. The red and purple L-shells point in the sun and dusk directions, respectively.

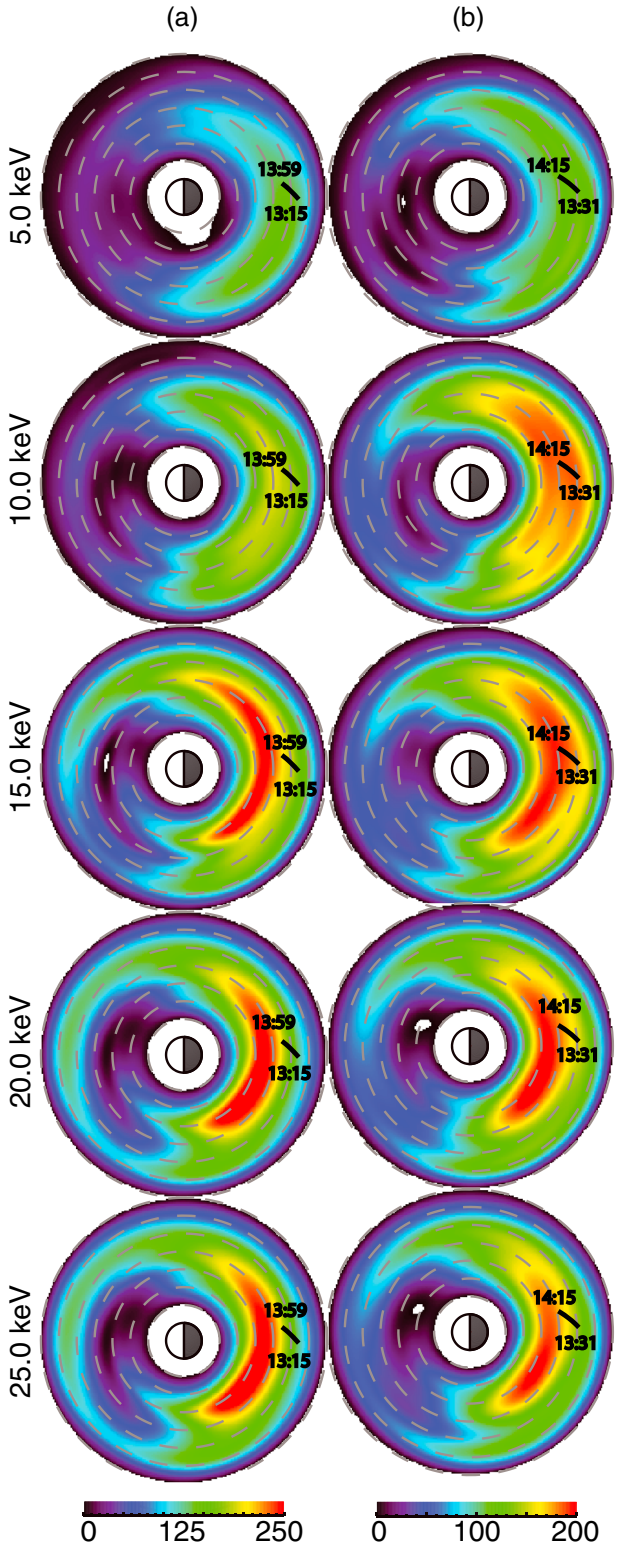

Figure 3. Deconvolved 5–25 keV equatorial ion intensity averaged over pitch angle for (a) 1330–1347 UT and (b) 1347–1404 UT. The dashed concentric circles indicate radii from 2 to 8 R_E. The ion intensities are plotted on a linear scale in units of [# of protons/(s cm^2 eV sr)] with the same colorbar for all energies during the two time periods. The paths of THEMIS D (E) from 1315 to 1359 (1331 to 1415) UT are also shown.

3. Observations

[12] In this study, we focus upon a half-hour period early in the recovery phase of a geomagnetic storm on 29 May 2010. This interval was selected because in addition to excellent TWINS-2 ENA images, THEMIS passes near the peak in the deconvolved ion distributions providing in situ comparison with the global plots. In this section, we present the relevant data. The interpretation and significance are presented in section 4.

[13] The interplanetary magnetic field data for the 29 May 2010 event is shown in the top panel of Figure 1. The absolute magnitude of the interplanetary magnetic field and the components B_x, B_y, and B_z in the GSM coordinate system are shown. The symmetric (SYM/H), the auroral electrojet (AE), and the antisymmetric (ASY/H) indices are shown in the bottom three panels of Figure 1 The geomagnetic storm evidenced in the negative excursion of the symmetric component of the ring current, SYMH, is likely caused by a CME driven storm; i.e., based upon the interplanetary field data, the driver is a magnetic flux rope in the solar wind. It should also be noted that 27 days prior to this storm, there was another storm which often indicates a corotating interaction region (CIR)-driven storm. The interval of interest, i.e., where we analyze TWINS-2 and THEMIS D and E observations in this study, is indicated in the figure by dashed vertical lines.

[14] The ENA images taken by the TWINS-2 instrument are shown in Figure 2. The images are 15-sweep, ~17 min averages, taken in energy intervals centered at 5, 10, 15, 20, and 25 keV with widths equal to the central energy; i.e., the 15 keV interval extends from 7.5 to 22.5 keV. These energies are chosen for direct comparisons of the deconvolved ion intensities with the THEMIS ESA instrument. The intensity is plotted on a log scale with a fixed color bar for each time interval to feature the energy dependence of the observed ENA emissions. The left column of ENA images covers the interval 1330 UT–1347 UT, and the right column covers 1347 UT–1405 UT. Note that the LAEs are the strongest emission, with extensive high altitude emissions in the tail. The ENA emissions on the dayside near noon are much less intense.

[15] The corresponding deconvolved equatorial ion intensities (averaged over pitch angle) are shown in Figure 3 in the SM coordinate system. The dashed concentric circles indicate radii from R = 2 R_E to R = 8 R_E. The ion intensities are plotted on a linear scale in units of [(# of protons)/(s cm^2 eV sr)] with the same colorbar for all energies during each time period. The THEMIS D and E paths are plotted for 1309–1407 UT and 1326–1425 UT, showing that each spacecraft moves from approximately R = 6.5 R_E to R = 4.5 R_E on the nightside. These times were chosen to correspond approximately to ±30 min from the center time (1338 UT, 1356 UT) of each TWINS image.

[16] The deconvolved ion intensities show peaks on the nightside and significant reduction near noon consistent with the diminished ENA flux at noon on a log scale of Figure 2. The ion intensities are stronger at 20 keV than 10 keV, whereas the reverse is true for the ENA images. This is due to (1) the energy dependence of the charge exchange cross section and thick target approximation for the LAEs and (2) the widths of the energy bands which extend from 5 to 15 (10–30) keV for the 10 (20) keV images and plots.

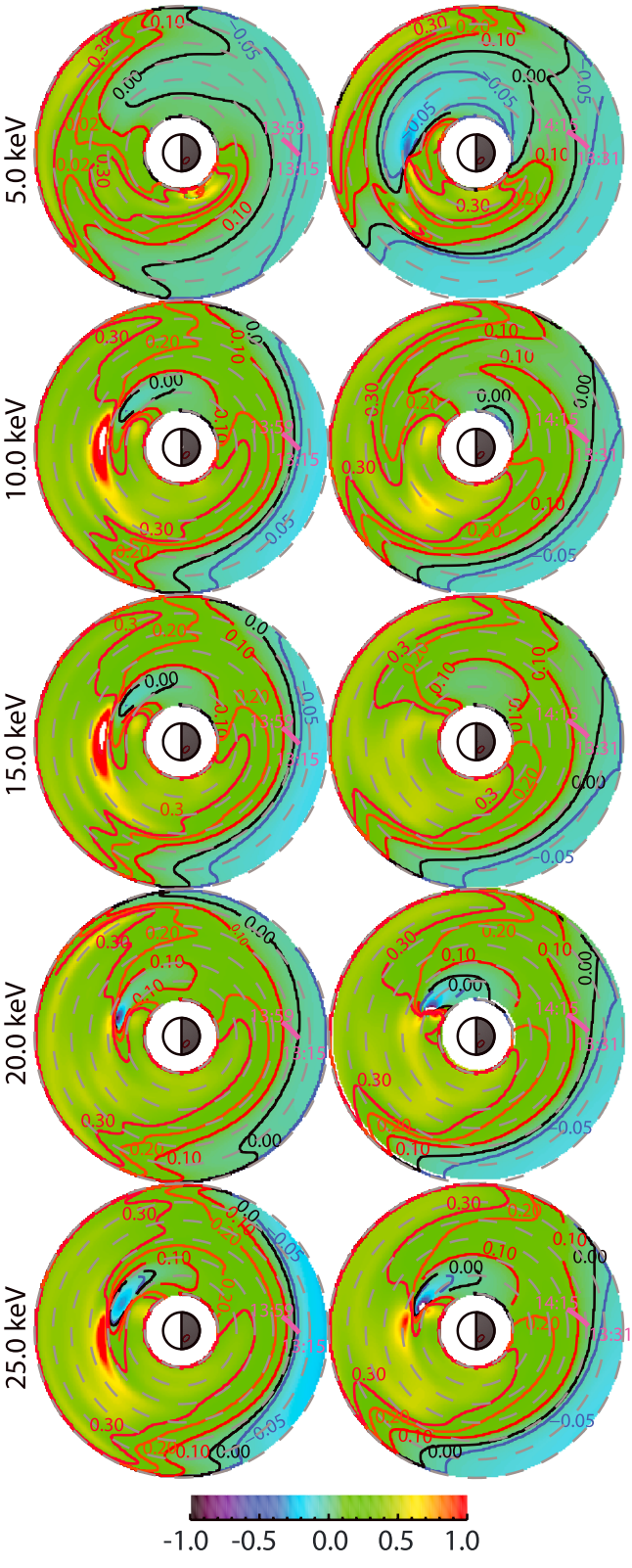

Figure 4. Deconvolved 5–25 keV equatorial pitch angle anisotropy in the same format as Figure 3. Labeled isocontours for anisotropies −0.05, 0.0, 0.1, 0.2, and 0.3 are also shown.

(Fordetails, please see *Perez et al.* [2012].) That the results are reasonable is demonstrated when the energy spectra are compared to THEMIS measurements (shown in *Perez et al.* [2012] and below in Figure 8).

[17] Figure 4 shows the corresponding deconvolved ion pitch angle anisotropy as a function of energy for (a) 1330 UT–1347 UT and (b) 1347 UT–1405 UT. Again, the THEMIS D (1309 UT–1407 UT) and THEMIS E (1326–1425 UT) paths are shown on the equatorial plots. To calculate the pitch angle anisotropy, A, we adopt a definition similar to that used by *Chen et al.* [1998],

$$A = \frac{I_\perp - 2I_{||}}{I_\perp + 2I_{||}}$$

$$I_\perp = \int_{-1}^{1} f_{eq} \sin^3\psi d\psi$$

$$I_{||} = \int_{-1}^{1} f_{eq} \cos^2\psi \sin\psi \, d\psi$$

where the $I_\perp(I_{||})$ emphasize the perpendicular (parallel) part of the pitch angle distribution, f_{eq} is the ion distribution function at the equator, and ψ is the ion pitch angle. Using this definition, a field-aligned distribution corresponds to −1, a perpendicular distribution corresponds to +1, and an isotropic distribution corresponds to 0. It should be noted that the strongly nonisotropic distributions observed in small regions on the day side correspond to areas with very low ion intensity as shown in Figure 3 and are not valid. The anisotropy in regions of appreciable ion intensity is close to zero, i.e., nearly isotropic or positive, i.e., somewhat perpendicular. Isocontours of the anisotropy illustrate gradients in the anisotropy reflecting regions in which the pitch angle distribution becomes more perpendicular.

[18] Figure 5a shows the fraction of pitch angles at $z = 0$ in the SM coordinate system (hereafter referred to as the SM equator) which are visible to the TWINS-2 instrument at its position for the time period 1330–1347 UT. Since the satellite position is not very different for the 1347–1404 UT period, only this plot is shown. The THEMIS D path during this time period is also shown. TWINS-2 is at height 6.07 R_E, latitude 62°, and 1244 MLT. For imaging lines of sight nearly normal to the SM equatorial plane; i.e., below the satellite, the fraction of visible pitch angles is smallest because ENAs created from ions with large pitch angles do not reach

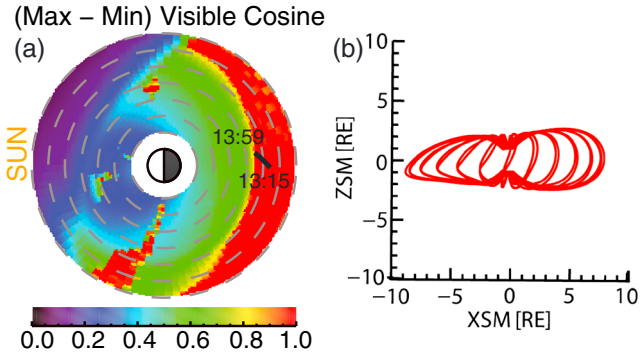

Figure 5. (a) Visible fraction of pitch angles in the SM equatorial plan for 1330–1347 UT. (b) Field lines from Tsy05 that intersect the SM equator at 8 R_E projected onto the x-z plane.

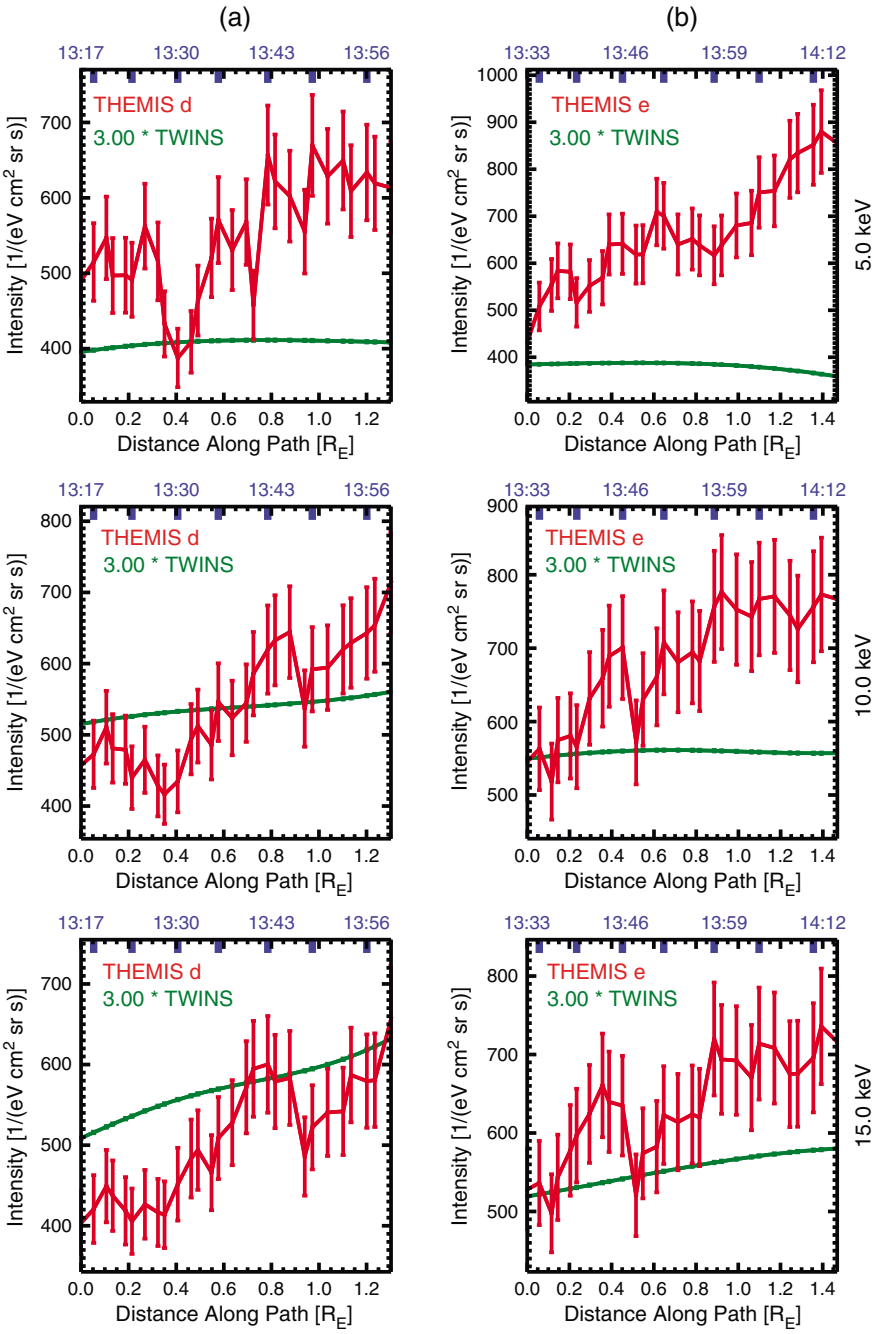

Figure 6. Comparison of the TWINS-2 and (a) THEMIS D, (b) THEMIS E ESA ion intensities along the THEMIS paths for 1331–1359 UT (Figure 6a) and 1331–1415 UT (Figure 6b). The UT time along the THEMIS path is shown in blue along the top *x* axis, and the distance along the path is shown along the bottom *y* axis.

the satellite. In the tail, ENAs with larger pitch angles are observable. Note that in some regions, shown in red, even pitch angles near 90° at the SM equator are visible. This is due to the fact that the Tsygenenko 2005 magnetic field model used in this study differs from a dipole in a manner so that the B field at the SM equator is not perpendicular to the SM *x-y* plane as shown in Figure 5b.

[19] In Figure 6, we show the ion intensity averaged over pitch angle along the THEMIS path at various energies for (a) THEMIS D and (b) THEMIS E. The TWINS-2 results are scaled by a factor 3 in order to compare the spatial (time) variations of the ion intensities obtained from the TWINS-2 ENA images and the THEMIS ESA measurements on a linear scale which is here used to provide a detailed comparison. This factor is chosen just to put the results on a comparable linear scale. This difference between the magnitude of the THEMIS and TWINS results is not understood at this time. It should be noted that comparison of ion intensities from inversions of ENA images from IMAGE/HENA also showed differences in magnitude [*Vallat et al.*, 2004]. The time along the THEMIS path is shown in blue along the top *x* axis, and the distance along the path is shown along the bottom *x* axis.

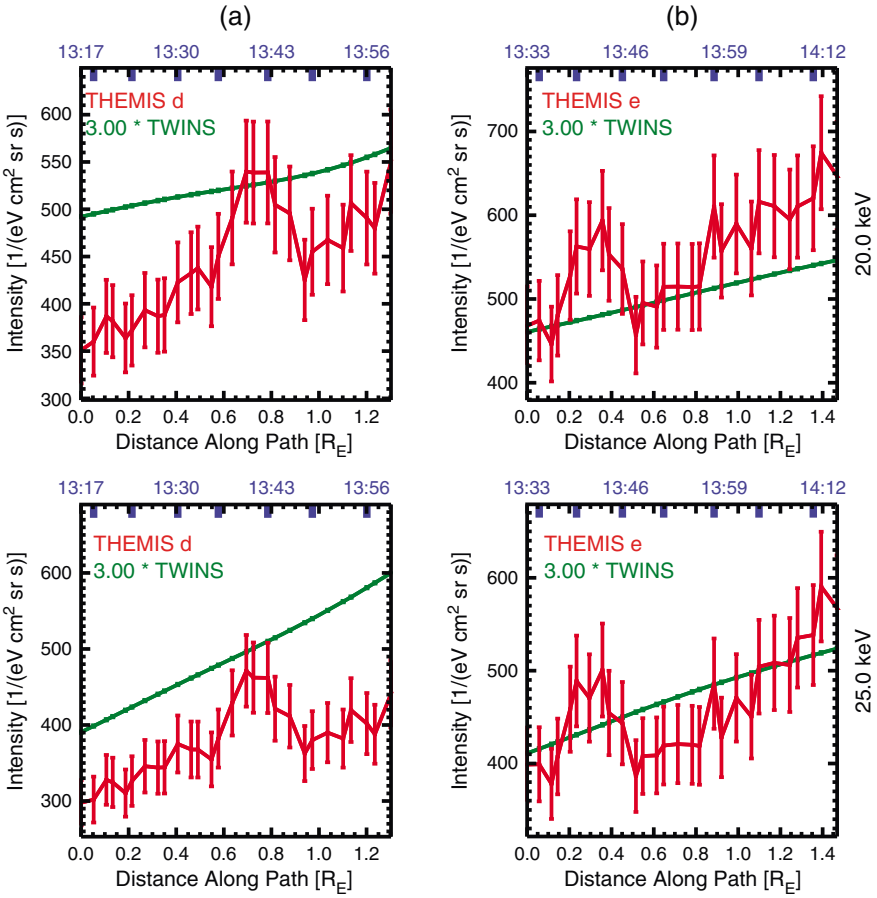

Figure 6. (continued)

The scaled THEMIS measurements are plotted in red with the TWINS-2 results plotted in green. Background is subtracted from the THEMIS measurements and error bars are estimated to be 10% of the ESA intensity to quantify uncertainty in the THEMIS measurements. The TWINS-2 error bars are very small because they only represent the estimated statistical error in the TWINS-2 measurements propagated through the deconvolution process [*Perez et al.*, 2012]. It should be noted that they do not include the errors due to factors such as uncertainties in the magnetic field model, geocoronal model, and spatial resolution of the TWINS instruments which are expected to be much larger but are difficult if not impossible to quantify. This issue was also addressed for ion intensities obtained from ENA images from IMAGE/HENA [*Vallat et al.*, 2004] and will be discussed further in section 4. These factors as well as the fact that if there are O^+ ions present they impact the TWINS and THEMIS measurements differently may contribute to an explanation of the disagreement in the overall magnitudes of the TWINS and THEMIS results. To compare the THEMIS measurements directly with the deconvolved equatorial ion intensities, the THEMIS distribution is mapped along magnetic field lines to the SM equator using the Tsy05 magnetic field model, while conserving the first adiabatic invariant.

[20] The equatorial pitch angle anisotropies along the THEMIS paths are shown for various energies in Figure 7. As with Figure 6, the (a) THEMIS D and (b) THEMIS E anisotropies are shown in red with comparisons with the deconvolved TWINS-2 anisotropies in green at (a) 1330–1347 UT and (b) 1347–1405 UT. The anisotropy is calculated in the same manner as Figure 4, with −1 representing a field aligned distribution, +1 representing a perpendicular distribution, and 0 being an isotropic distribution.

[21] In Figure 8, we show a comparison of the deconvolved ion spectrum with the spectrum observed by (a) THEMIS D and (b) THEMIS E. For both cases, we make the comparison at the time corresponding to the middle of the TWINS observations, so (a) from 1330 to 1347 UT the comparison is made with THEMIS D at 1338 UT and (b) from 1347 to 1405 UT the comparison is made with THEMIS E at 1356 UT. The blue points at every 5 keV represent the ion intensities directly from the deconvolution. The horizontal bars on the blue ion intensities represent the width of the energy band at each energy; the vertical error bars represent the statistical errors from the deconvolution process. The red lines represent the energy spectrum from the deconvolution process after taking into account the wide energy bands at each energy by making a linear expansion of the energy spectrum in terms of cubic B-splines and solving for the unknown coefficients using singular value decomposition [*Perez et al.*, 2012]. The brown points are the intensities from the THEMIS ESA and SST instruments. In order to emphasize the comparison of the spectral shapes, the TWINS results were normalized to have the same maximum value as the THEMIS measurements. The THEMIS error bars are again estimated to be 10% of the original intensity.

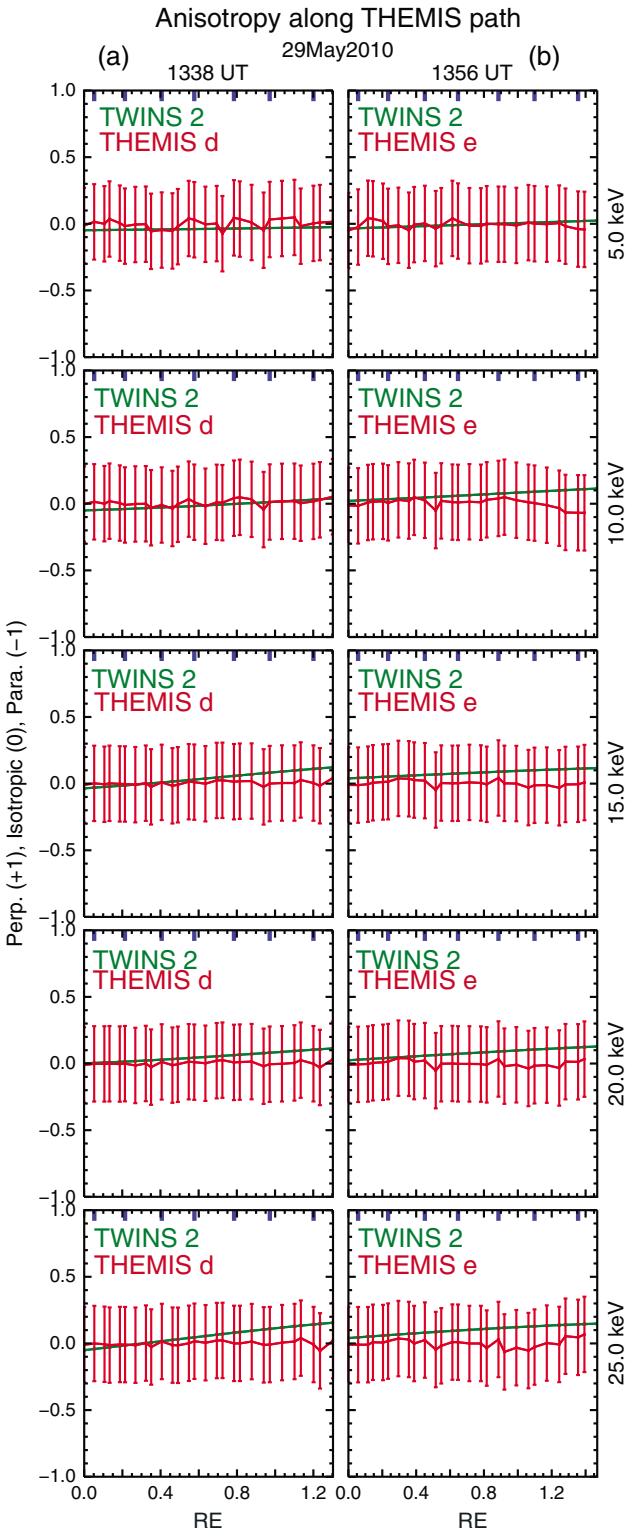

Figure 7. Comparison of the TWINS-2 and (a) THEMIS D, 1315–1359 UT, and (b) THEMIS E, 1331–1415 UT, ESA ion pitch angle anisotropy along the THEMIS paths. The red bars are based on the 10% error estimates for the THEMIS intensity.

[22] The pitch angle anisotropy shown in Figures 4 and 7 are from the distribution function at the SM equator. As is shown in Figure 5b, the point of minimum B along field lines in the tail outside of L = 6 R_E is displaced from the SM equator. Pitch angles near 90° at the point of minimum B mirror before reaching the SM equator. Therefore, to compare the energy-dependent pitch angle distributions (PADs) obtained from TWINS-2 with those measured by THEMIS during the time periods of interest, we have mapped both PADs to the point of minimum B, not the SM equator. The results are shown in Figure 9.

[23] To make a direct comparison of the shape of each distribution, the pitch angle distribution for each instrument is normalized so that the integral over the pitch angle of each PAD is unity, i.e.,

$$PAD(\psi)_{\text{normalized}} = \frac{PAD(\psi)}{\int_{-1}^{1} PAD(\psi)\, d\psi}$$

[24] Each THEMIS data point has an error bar representing 10% of the intensity. The dashed vertical blue lines indicate the range of pitch angles at the location of minimum B visible to TWINS at these specific observing locations. We note that for the time 1338(1356) UT, pitch angles larger than 60° (70°) are not seen by TWINS-2 from its position at that time.

[25] It is to be noted that for the quantity plotted in Figure 9, an isotropic distribution has sin ψ dependence. It is not a constant. This means that the area under the curve, i.e., the integral over ψ, is proportional to the number of particles [*Parker*, 1957].

4. Discussion

[26] This event was chosen for detailed analysis due to the combination of the relatively high level of geomagnetic activity and coincident observation locations of TWINS-2 and the two THEMIS spacecraft. The fact that the path of THEMIS spacecraft passed through or near the peak in the deconvolved distribution makes this interval an especially interesting time for comparison with the global measurements. THEMIS makes detailed in situ measurements, and TWINS provides a lower resolution but global view not easily attained in another way at this time.

[27] These observations occur during the early recovery phase of the storm on 29 May 2010, as indicated by the SYM/H index in Figure 1. The ENAs in Figure 2 as well as the TWINS 2 deconvolved equatorial ion intensities in Figure 3 indicate that even though we are in the recovery phase of this storm, the ring current has not yet symmetrized. This is consistent with the elevated ASY/H index in the bottom panel of Figure 1 and with previous ENA observations [*Pollock et al*., 2001]. *Liemohn et al*. [2001] give an extensive description of observations and modeling of this feature of the ring current.

[28] In Figure 2, there ENA emissions from both low and high altitudes are seen.. The brightest pixels occur from the LAEs due to the higher neutral oxygen density at low altitudes. These LAEs are likely due to a precipitating ring current population near midnight. This convenient viewing geometry provides measurements of nearly the entire range of equatorial pitch angles in the SM coordinate system on

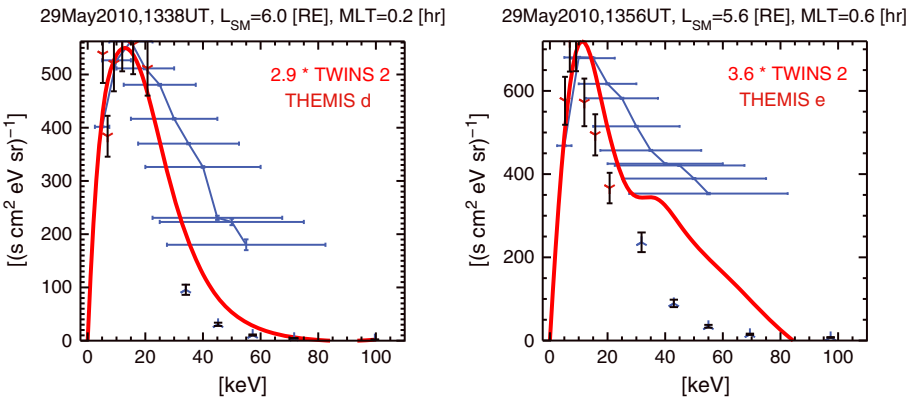

Figure 8. Comparison of the TWINS-2 and (a) THEMIS D, (b) THEMIS E ion spectra for 5–55 keV. The blue points at 5 keV intervals represent the ion intensities directly from the deconvolution (see Figure 3). The horizontal bars on the blue ion intensities represent the width of the energy band at each point; the vertical error bars represent the statistical errors from the deconvolution process. The red lines represent the energy spectrum having taken into account the wide energy bands [*Perez et al.*, 2012]. The brown points are the intensities from the THEMIS ESA and SST instruments. The TWINS-2 intensities were scaled so the peaks have the same value as the THEMIS data.

the nightside as seen by the fraction of pitch angles visible to TWINS-w at this location in Figure 5.

[29] For both observation intervals, the deconvolved equatorial ion intensity shown in Figure 3 peaks between 4 and 5 R_E on the nightside for energies 15–25 keV and slightly further out for 5–10 keV. This is consistent with the relatively more intense high altitude emissions at 5–10 keV observed in the ENAs (see Figure 2.).

[30] The global plots of pitch angle anisotropy in Figure 4 are only available from measurement techniques like ENA imaging. Some previous in situ measurements in the ring for L = 3–5 R_E for all MLT values at energies from 24.0 to 44.5 keV [*Garcia and Spjeldvik*, 1985] characterized the anisotropy by fitting the function $\sin^n\psi$ to observations by ISEE 1 from November 1977 to December 1978. They found values of n that varied from 4 at L near 3 to 2 at L near 5 with considerable scatter in the data. These n values correspond to 0.35–0.45 for the anisotropy plotted in Figure 4. The somewhat higher values from ISEE 1 may well be due to the higher energy range in those measurements [*Chen et al.*, 1998; *Fritz et al.*, 2003], but the results presented here show the same trend of higher anisotropy for lower L values.

[31] The positive values of the anisotropy in Figure 4 are indicative of ion distribution functions with $T_\perp > T_\parallel$. *Gary et al.* [1994] used linear theory and simulations to show that for high enough $T_\perp > T_\parallel$, electromagnetic proton cyclotron anisotropy instability may be generated. The resulting electromagnetic ion cyclotron waves (EMIC) can lead to pitch angle scattering causing precipitation of the ions with small pitch anglex [*Kennel and Petschek*, 1966]. This is a possible explanation of the rising anisotropy near dusk and the decrease in the pitch angle averaged intensity of the trapped ring current ions as shown in Figure 4. This is an example of how the global pitch angle information available from TWINS ENA images may contribute to a better understanding of the lifetimes of trapped ring current ions.

[32] The spatial dependence of the energy-dependent ion intensity along the THEMIS paths shown in Figure 6 shows that the TWINS ENA images cannot resolve the details of the spatial structure observed by THEMIS. But the TWINS results do match the spatial trends. The spike in ion intensity observed by THEMIS E just after 1420 UT occurs after the TWINS-2 observations have ended and could be due to either an injection of plasma into the ring current after 1420 UT or movement to lower L values of the inner edge of the plasma sheet [*Lui et al.*, 1987]. It should be noted that the TWINS results were multiplied by 3 to put them on the same scale as the THEMIS results and that the magnitude of this factor is not understood at this time. One possible contributing factor would be O^+ ions being mixed in with the dominant H^+ as the two instruments respond very differently to the O^+, THEMIS being an energy measurement and TWINS a velocity measurement. The THEMIS results for very similar paths for different time intervals show a small but consistent increase in intensity with time. This trend is also seen in the TWINS results.

[33] The energy-dependent anisotropy along the THEMIS paths shown in Figure 7 shows values that are consistent between the two measurements. It is to be noted that for the definition used in this study, the anisotropy is independent of the overall magnitude of the intensity. It depends only on the shape of the pitch angle distribution (see the definition of A in section 3 above). It is also to be noted that the TWINS results show an increase in the anisotropy along the path; i.e., anisotropy increases with smaller L. This is consistent with the results of *Garcia and Spjeldvik* [1985], *Chen et al.* [1998], and *Fritz et al.* [2003] described above. The comparison of the ion energy spectrum obtained from THEMIS and TWINS shown in Figure 8 shows peaks at similar energies, implying similar temperatures. As in Figure 6, the magnitude of the TWINS intensity has been multiplied by a factor. This time, however, a specific factor was chosen to match the peaks in the spectra in order to facilitate the comparison of the spectral shapes. At the earlier time, both instruments show similar energy tails, but at the later time, the TWINS spectrum shows a clear high energy tail not evident in the THEMIS measurement.

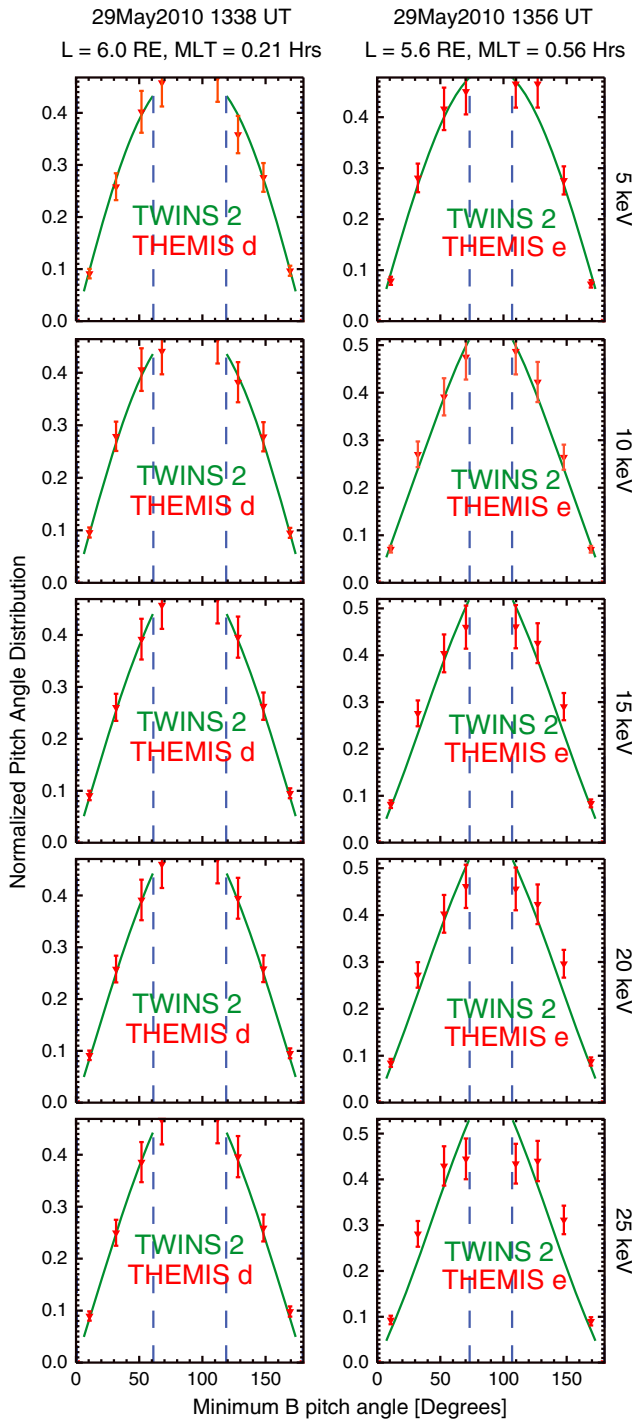

Figure 9. Comparison of the TWINS-2 (green) and THEMIS D (E) (red) PADs for 5, 10, 15, 20, and 25 keV at 1338 (1356) UT at L = 6.1 (5.6) R_E, MLT = 0.21 (0.56) h. The PADS are normalized to unit area.

[34] The agreement of the shape of the pitch angle distribution as seen in Figure 9 is generally excellent and provides confidence in the global map of pitch angle anisotropy in Figure 4. The one exception appears at pitch angles close to 90° in the higher energies of the in situ measurements during the 1347 UT–1405 UT interval, when THEMIS E is at L = 5.6 R_E, MLT = 0.56 (see right column in Figure 9). For the TWINS pitch angle distribution from 0° to 90°, the deconvolution uses splines as cubic polynomials in cos(ψ) to fit the observations. When the results are nearly straight lines, the penalty function in the deconvolution process has reduced a polynomial of degree 3 to one of degree 1. This means that there is not enough information content, i.e., ENA intensity and the estimated uncertainties, in the ENA images to obtain the entire shape of the pitch angle distribution.

5. Summary

[35] In summary, we have shown the first direct comparisons of global and in situ ion intensities and their respective pitch angle distributions in the ring current during the early recovery phase of a geomagnetic storm on 29 May 2010. We have also shown how the equatorial ion intensity and pitch angle anisotropy varies as a function of L and MLT and energy in the ring current. For the interval in this study, the equatorial ion intensity is antisymmetric with the peak near L = 4–5 R_E close to midnight.

[36] The global maps of pitch angle anisotropy show pitch angle distributions that are more perpendicular than parallel consistent with $T_\perp > T_\parallel$ and show features consistent with previous measurements and model calculations and simulations. The anisotropy obtained from TWINS ENA images shows a somewhat larger value than that measured by THEMIS at smaller L values. Detailed comparison with the pitch angle distribution at times at the center of the ENA images, however, shows good agreement. The global variation of pitch and anisotropy obtained from the TWINS ENA images provides information that will help improve the understanding of the lifetime of ions trapped in the ring current.

[37] **Acknowledgments.** The authors would like to acknowledge Natalia Papitashvili at the Space Physics Data Facility at NASA Goddard Spaceflight Center for use of the OMNI data set as well as the THEMIS ESA and SST teams for use of the THEMIS data and software. This work was carried out as a part of and with support from the TWINS mission as a part of NASA's Explorer Program.

References

Angelopoulos, V., et al. (2008), The THEMIS mission, *Space Sci. Rev.*, *141*(1–4), 5–34, doi:10.1007/s11214-008-9336-1.

Barnett, C. F. (1990), Atomic Data for Fusion, Volume 1: Collisions of H, H2, He, and Li Atoms and Ions with Atoms and Molecules, Technical Report ORNL-6086/V1, Oak Ridge National Laboratory, Oak Ridge, Tenn.

Bazell, D., E. C. Roelof, T. Sotirelis, P. C. Brandt, H. Nair, P. Valek, J. Goldstein, and D. McComas (2010), Comparison of TWINS images of low-altitude emission of energetic neutral atoms with DMSP precipitating ion fluxes, *J. Geophys. Res.*, *115*, A10204, doi:10.1029/2010JA015644.

C:son Brandt, P., S. Barabash, O. Norberg, R. Lundin, E. C. Roelof, C. J. Chase, B. H. Mauk, and M. Thomsen (1997), ENA imaging from the Swedish micro satellite Astrid during the magnetic storm of 8 February, 1995, *Adv. Space Res.*, *20*(4–5), 1061–1066.

Chen, M. W., J. L. Roeder, J. F. Fennell, L. R. Lyons, and M. Schulz (1998), Simulations of ring current proton pitch angle distributions, *J. Geophys. Res.*, *103*(A1), 165–178, doi:10.1029/97JA02633.

deBoor, C. (1978), *A Practical Guide to Splines*, Springer-Verlag, N.Y.

Ebihara, Y., M.-C. Fok, T. J. Immel, and P. C. Brandt (2011), Rapid decay of storm time ring current due to pitch angle scattering in curved field line, *J. Geophys. Res.*, *116*, A03218, doi:10.1029/2010JA016000.

Fritz, T. A., M. Alothman, J. Bhattacharjya, D. L. Matthews, and J. Chen (2003), Butterfly pitch-angle distributions observed by ISEE-1, *Planet. Space Sci.*, *51*, 205–219.

Garcia, H. A., and W. N. Spjeldvik (1985), Anisotropy characteristics of geomagnetically trapped ions, *J. Geophys. Res.*, *90*(A1), 347–358, doi:10.1029/JA090iA01p00347.

Gary, S. P., M. B. Moldwin, M. F. Thomsen, D. Winske, and D. J. McComas (1994), Hot proton anisotropies and cool proton temperatures in the outer magnetosphere, *J. Geophys. Res.*, *99*, 23,603–23,615, doi:10.1029/94JA02069.

Goldstein, J., P. Valek, D. J. McComas, and J. Redfern (2012a), Latitudinal anisotropy in ring current energetic neutral atoms, *Geophys. Res. Lett.*, *39*, L08102, doi:10.1029/2012GL051417.

Goldstein, J., P. Valek, D. J. McComas, and J. Redfern (2012b), TWINS energetic neutral atom observations of local-time-dependent ring current anisotropy, *J. Geophys. Res.*, *117*(A11), A11213, doi:10.1029/2012JA017804.

Grimes, E. W., J. D. Perez, J. Goldstein, D. J. McComas, and P. Valek (2010), Global observations of ring current dynamics during CIR-driven geomagnetic storms in 2008, *J. Geophys. Res.*, *115*(A11), A11207, doi:10.1029/2010JA015409.

Kennel, C. F., and H. E. Petschek (1966), Limit of stably trapped particle fluxes, *J. Geophys. Res.*, *71*, 1–28.

Liemohn, M. W., J. U. Kozyra, M. F. Thomsen, J. L. Roeder, G. Lu, J. E. Borovsky, and T. E. Cayton (2001), Dominant role of the asymmetric ring current in producing the stormtime Dst, *J. Geophys. Res.*, *106*, 10,883–10,904.

Lui, A. T. Y., R. W. McEntire, and S. M. Krimigis (1987), Evolution of the ring current during two geomagnetic storms, *J. Geophys. Res.*, *92*(A7), 7459–7470, doi:10.1029/JA092iA07p07459.

McComas, D. J., et al. (2009a), The Two Wide-angle Imaging Neutral-atom Spectrometers (TWINS) NASA Mission-of-Opportunity, *Space Sci. Rev.*, *142*, 157–231, doi:10.1007/s11214-008-9467-4.

McComas, D. J., et al. (2009b), Global observations of the interstellar interaction from the Interstellar Boundary Explorer (IBEX), *Science*, *326*(5955), 959–962, doi:10.1126/science.1180906.

McComas, D. J., N. Buzulukova, M. G. Connors, M. A. Dayeh, J. Goldstein, H. O. Funsten, S. Fuselier, N. A. Schwadron and P. Valek (2012), Two Wide-Angle Imaging Neutral-Atom Spectrometers and Interstellar Boundary Explorer energetic neutral atom imaging of the 5 April 2010 substorm, *J. Geophys. Res.*, *117*, A03225, doi:10.1029/2011JA017273.

McFadden, J. P., C. W. Carlson, D. Larson, J. Bonnell, F. Mozer, V. Angelopoulos, K.-H. Glassmeier, and U. Auster (2008), THEMIS ESA first science results and performance issues, *Space Sci. Rev.*, doi:10.1007/s11214-008-9433-1.

Østgaard, N., S. B. Mende, H. U. Frey, G. R. Gladstone, and H. Lauche (2003), Neutral hydrogen density profiles derived from geocoronal imaging, *J. Geophys. Res.*, *108*(A7), 1300, doi:10.1029/2002JA009749.

Parker, E. N. (1957), Newtonian development of the dynamical properties of ionized gases of low density, *Phys. Rev.*, *10*, 924–933.

Perez, J. D., E. W. Grimes, J. Goldstein, D. J. McComas, P. Valek, and N. Billor (2012), Evolution of CIR storm on 22 July 2009, *J. Geophys. Res.*, *117*, A09221, doi:10.1029/2012JA017572.

Pollock, C. J., et al. (2001), First medium energy neutral atom (MENA) images of Earth's magnetosphere during substorm and storm-time, *Geophys. Res. Lett.*, *28*, 1147–1150.

Roelof, E. C. (1987), Energetic neutral atom image of a storm-time ring current, *Geophys. Res. Lett.*, *14*(6), 652–655, doi:10.1029/GL014i006p00652.

Tsyganenko, N. A., and M. I. Sitnov (2005), Modeling the dynamics of the inner magnetosphere during strong geomagnetic storms, *J. Geophys. Res.*, *110*, A03208, doi:10.1029/2004JA010798.

Valek, P., P. C. Brandt, N. Buzulukova, M.-C. Fok, J. Goldstein, D. J. McComas, J. D. Perez, E. Roelof, and R. Skoug (2010), Evolution of low altitude and ring current ENA emissions from a moderate magnetospheric storm: Continuous and simultaneous TWINS observations, *J. Geophys. Res.*, *115*, A111209, doi:10.1029/2010JA015429.

Vallat, C., et al. (2004), First comparisons of local ion measurements in the inner magnetosphere with energetic neutral atom magnetospheric image inversions: Cluster-CIS and IMAGE-HENA observations, *J. Geophys. Res.*, *109*, A04213, doi:10.1029/2003JA010224.

Wahba, G. (1990), *Spline Models for Observational Data*, Society for Industrial and Applied Mathematics, Philadelphia, Pa.

Xiao, F., Q. Zhou, H. He, H. Zheng, and S. Wang (2007), Electromagnetic ion cyclotron waves instability threshold condition of suprathermal protons by kappa distribution, *J. Geophys. Res.*, *112*, A07219, doi:10.1029/2006JA012050.

Zheng, Y., A. T. Y. Lui, and M.-C. Fok (2008), Viewing perspective in energetic neutral atom intensity, *J. Geophys. Res.*, *113*, A09217, doi:10.1029/2008JA013070.